Studying dark matter using weak gravitational lensing : from galaxies to the cosmic web

Brouwer, M.M.

Author: Brouwer, Margot
Title: Studying dark matter using weak gravitational lensing : from galaxies to the cosmic web
Date: 2017-12-20

4 Trough Lensing with KiDS, GAMA and MICE

Based on: "A weak lensing study of troughs using the KiDS, GAMA and MICE galaxy catalogues" *(in preparation)*
Authors: Margot M. Brouwer *et al.*

Abstract:
We study projected underdensities in the cosmic galaxy density field called 'troughs', and their overdense counterparts which we call 'ridges'. For their classification we use a bright sample of foreground galaxies from the photometric Kilo-Degree Survey (KiDS), specifically selected for comparison to the spectroscopic Galaxy And Mass Assembly (GAMA). Using an independent sample of KiDS background galaxies, we measure the weak gravitational lensing profiles of the troughs and ridges. We quantify the amplitude A of the lensing signal as a function of their galaxy density percentile P and overdensity δ, and use this to optimally stack the signal, which is detected with a signal to noise of $|S/N| = \{17.1, 14.8, 10.0, 7.6\}$ for troughs with a projected radius $\theta_{\rm A} = \{5, 10, 15, 20\}$ arcmin. We find that the skewness in the galaxy density distribution of troughs/ridges is reflected in the total mass distribution measured by weak lensing. We compare our results by applying the same procedures to a mock galaxy sample from the MICE Grand Challenge lightcone simulation, and find a good agreement between our observations and the simulation. Finally, we select troughs using a volume limited sample of galaxies, divided into two redshift bins between $0.1 < z < 0.3$. For troughs/ridges with comoving projected radius $R_{\rm A} = 1.9\, h_{70}^{-1}{\rm Mpc}$, we find no significant difference between the $A(P)$ and $A(\delta)$ relation of the low and high redshift sample. Using the MICE simulations we predict that trough and ridge evolution could be detected with lensing, using deeper and more accurate lensing surveys.

4.1 Introduction

Over the past two decades, large scale galaxy redshift surveys, such as the 2dF Galaxy Redshift Survey (2dFGRS, Colless et al. 2001) and the Sloan Digital Sky Survey (SDSS, Abazajian et al. 2009) have provided an accurate picture of the distribution of galaxies in the Universe. They show that galaxies form an intricate 'cosmic web' of clusters and filaments, separated by largely empty regions named voids. This distribution is also observed in large scale simulations based on the concordance ΛCDM cosmology, such as the Millennium (Springel et al. 2005b), Illustris (Vogelsberger et al. 2014) and EAGLE (Schaye et al. 2015) projects, which show the gravitational collapse of dark matter (DM) into a web-like structure, establishing the 'skeleton' for baryonic matter which falls into the DM's potential well. Within this framework, the linear growth factor of voids with redshift can be used to constrain the equation of state parameter of dark energy (DE) (Lavaux and Wandelt 2010; Demchenko et al. 2016), which causes the Universe's accelerated expansion. The low density in voids also ensures that they are very clean probes of global cosmological parameters, as their interior is less affected by baryonic physics (Bos et al. 2012). In addition to testing the standard model of cosmology, voids can also be used to detect signatures of modified gravity models, which aim to provide an alternative explanation to the accelerating expansion of the Universe (for reviews, see Jain and Khoury 2010; Clifton et al. 2012). Because these theories should converge to standard general relativity inside the solar system, most implement a screening mechanism that suppresses their '5^{th} force' in high density regions. Simulations based on modified gravity show that low density regions, like voids, are excellent probes for testing these theories (Li et al. 2012; Lam et al. 2015; Zivick et al. 2015).

Studying, detecting, or even defining voids, however, is not a simple matter. There exist numerous void finding algorithms, each one operating with a different void definition (for a comparison study, see e.g. Colberg et al. 2008). Secondly, applying the algorithm of choice to detect voids in observational data requires very accurate redshift measurements of every individual galaxy. Such accuracy is only available through complete spectroscopic surveys, which are far more costly than their photometric counterparts. Finally, the true DM structure of voids can be different than that of the galaxies that trace them, an effect known as 'galaxy bias' (Benson et al. 2000; Tinker et al. 2010). Currently, the only way to study the total mass distribution of voids is through 'gravitational lensing', a statistical method that measures the gravitational deflection (or 'shear' γ) of the light of background galaxies (sources) by foreground mass distributions (lenses). The first detection of the lensing signal from cosmic voids was presented by Melchior et al. (2014), who stacked the gravitational shear around 901 voids detected in SDSS. The depth of their void lensing signal corresponded to the prediction from the analytical model by Krause et al. (2013), who concluded that lensing measurements of medium-sized voids with sufficient precision (i.e. with a signal to noise $S/N \gtrsim 10$) will only be possible with Stage IV surveys such as the Euclid satellite (Laureijs et al. 2011) and the Large Synoptic Survey Telescope (LSST, Dark Energy Science Collaboration 2012). One of the reasons this signal is so difficult to measure, is that the lensing method measures the average density contrast over the entire line-of-sight (LOS). If a dense cluster is located in the same LOS as the void, it can diminish the lensing signal. Another problem of studying voids using their stacked gravitational lensing signal is that this method only measures the average shear as a function of the projected radial distance from the void centre (Hamaus et al. 2014; Nadathur et al. 2015). This means that the detailed detection of void shapes is rendered superfluous, since this information will not be captured. Stacking voids that are not radially symmetric can even diminish the lensing signal. Moreover, the centre and the radius of these non-spherical voids are difficult to define, and choosing the wrong value reduces the lensing signal even further (for an analysis of these effects, see e.g. Cautun et al. 2016).

To circumvent the aforementioned problems, Gruen et al. (2016) (hereafter G16) constructed a definition for projected voids named 'troughs'. These are very simply defined as the most underdense circular regions on the sky, in terms of galaxy number density. Being circular in shape, troughs evade the problem of the centre definition, and are perfectly suited for measuring their stacked shear as a function of radial distance. Because they are defined as *projected* circular regions of low galaxy density, they can also be described in 3D as voids which have the shape of long conical frusta[1] protruding into the sky. Because this definition only includes regions that are underdense over the entire LOS, it automatically excludes LOS's with overdensities massive enough to negate the lensing measurement. Moreover, defining underdensities in projected space alleviates the need for spectroscopic redshifts. Even when projected underdensities are defined in a number of redshift slices, as was done by e.g. Sánchez et al. (2017), photomet-

[1]Frusta, the plural form of frustum: the part of a solid, such as a cone or pyramid, between two (usually parallel) cutting planes.

ric redshifts are sufficiently accurate as long as the slices are significantly wider than the redshift uncertainties. In short, the disadvantage of troughs compared to 3D voids is losing the shape information in both projected and redshift space, while their advantage is that they are specifically designed to allow for significant lensing measurements with currently available surveys. Following this new underdensity definition, G16 defined a set of $\sim 110,000$ troughs in the redMaGiC (Rozo et al. 2016) sample of Luminous Red Galaxies (LRGs). Using the Dark Energy Survey (DES, Flaugher et al. 2015) Science Verification Data, they measured the gravitational lensing signal of projected cosmic underdensities with a significance above 10σ, much higher than was ever measured around 3D voids.

The ways in which this new probe can be used for cosmology are still under examination. In the work of G16, they found the trough shear measurements to be in agreement with their theoretical model, which was based on the assumption that galaxies are biased tracers in a Gaussian mass density distribution. Although the lensing profile of their smallest troughs was marginally sensitive to galaxy bias, the trough-galaxy angular correlation function allowed for much stronger constraints. In their more recent paper Gruen et al. (2017) studied the probability distribution function (PDF) of large-scale matter density fluctuations, using the galaxy counts and lensing profiles of under- and overdensities along the LOS, obtained from the DES First Year and SDSS data. Using these troughs and overdensities, they were able to constrain the total matter density $\Omega_{\rm m}$, the power spectrum amplitude σ_8, the galaxy bias, galaxy stochasticity and the skewness of the matter density PDF. Another very promising venue for trough lensing is to test models of modified gravity. Using ray-tracing simulations Higuchi and Shirasaki (2016) found that, while 3D voids could not distinguish between $f(R)$ and ΛCDM even in future ($\sim 1000\,\deg^2$) lensing surveys, the lensing profiles from troughs showed a clear deviation. A recent comparison from Cautun et al. (2017) also found that the shear profiles of projected (2D) underdensities can constrain chameleon $f(R)$ gravity with confidence levels of up to ~ 30 times higher than those of 3D void profiles, using Euclid and LSST. For another type of modified gravity, the normal branch of the Dvali-Gabadadze-Porrati (nDGP) model, Barreira et al. (2017) found that it strenghtened the lensing signal of both projected under- and overdensities. In conclusion, the promise of projected underdensities for cosmology compels the weak lensing community to observationally explore these new probes, especially in preparation for future surveys such as Euclid and LSST.

Our goal is to measure and study the lensing profiles of troughs using the spectroscopic Galaxy And Mass Assembly survey (GAMA, Driver et al. 2011) and photometric Kilo-Degree Survey (KiDS, de Jong et al. 2013), following up on the work by G16. In particular we study troughs as a function of their galaxy number density, and try to find the optimal method of stacking their lensing signal to obtain the highest possible detection significance. We will compare our observed lensing profiles with mock observations devised by the Marenostrum Institut de Ciències de l'Espai (MICE) collaboration: the MICE Galaxy and Halo Light-cone catalogue (Carretero et al. 2015; Hoffmann et al. 2015), based on the MICE Grand Challenge lightcone simulation (MICE-GC, Fosalba et al. 2015b,a; Crocce et al. 2015). G16 also studied the lensing signals of troughs as a function of redshift, by splitting the LRG sample that defined the troughs into two redshift samples. However, they did not account for possible differences between the galaxy samples or trough geometry at different redshifts, nor did they correct for the variation in distance between the troughs and the background sources that measured the lensing signal. As a result, they did not find any signs of *physical* redshift evolution of troughs. By correcting the trough selection method and lensing signal measurement for all known differences between the two redshift samples, we explore the physical evolution of troughs.

Our paper is structured as follows: In Sect. 4.2 we introduce the KiDS and GAMA data used to define the troughs and measure their lensing profiles, and the MICE-GC mock data which we use to interpret our observations. Section 4.3 describes the classification of troughs, and explains the gravitational lensing method in detail. In Sect. 4.4 we show the resulting trough lensing profiles as a function of galaxy density and size, and define our optimal trough stacking method. Our study of troughs as a function of redshift is described in Sect. 4.5. We end with the discussion and conclusion in Sect. 4.6.

Throughout this work we adopt the cosmological parameters used in creating the MICE-GC simulations: $\Omega_{\rm m} = 0.25$, $\Omega_{\Lambda} = 0.75$, and $H_0 = 70\,{\rm km\,s^{-1}Mpc^{-1}}$. We use the following definition for the reduced Hubble constant: $h_{70} \equiv H_0/(70\,{\rm km\,s^{-1}Mpc^{-1}})$.

4.2 Data

We use two samples of foreground galaxies to define the locations of troughs: one sample from the spectroscopic GAMA survey and one from the photometric KiDS survey. Comparing the results obtained from these two samples allows us to test the strength and reliability of trough studies using only photometric data. In Table 4.1 we give a summary of the galaxy selections used to define the troughs. The gravitational lensing signal of these troughs is measured using a sample of KiDS background galaxies. The combination of the KiDS and GAMA datasets and the lensing measurement method, which is used for the observations described in this work, closely resemble those used in earlier KiDS-GAMA galaxy-galaxy lensing (GGL) papers. For more information we recommend reading Sect. 3 of Viola et al. (2015), which discusses the GGL technique in detail, and Dvornik et al. (2017) which makes use of exactly the same versions of the KiDS and GAMA datasets as this work. In order to compare our observational results to predictions from simulations, the same process of selecting troughs and measuring their lensing profiles will be performed using the MICE-GC mock galaxy catalogue. In this section we introduce the KiDS, GAMA and MICE galaxy catalogues, including their role in the trough selection and lensing measurement.

4.2.1 KiDS source galaxies

In order to derive the mass distribution of troughs, we measure their gravitational lensing effect on the images of background galaxies. Observations of these source galaxies are taken from KiDS, a photometric lensing survey in the u, g, r and i bands, performed using the OmegaCAM instrument (Kuijken 2011) mounted on the VLT Survey Telescope (Capaccioli and Schipani 2011). For this work we use the photometric redshift, magnitude, and ellipticity measurements from the third data release (KiDS-DR3, de Jong et al. 2017), which were also used for the KiDS-450 cosmic shear analysis (Hildebrandt et al. 2017). These measurements span $454\,\mathrm{deg}^2$ on the sky, and completely cover the $180\,\mathrm{deg}^2$ equatorial GAMA area.

The galaxy ellipticity measurements are based on the r-band observations, which have superior atmospheric seeing constraints (a maximum of 0.8 arcsec) compared to the other bands (de Jong et al. 2017). The galaxies are located by the SExtractor detection algorithm (Bertin and Arnouts 1996) from the co-added r-band images produced by the Theli pipeline (Erben et al. 2013). The ellipticity of each galaxy is measured using the self-calibrating *lens*fit pipeline (Miller et al. 2007, 2013b; Fenech Conti et al. 2017). Galaxies in areas surrounding bright stars or image defects (such as read-out spikes, diffraction spikes and reflection haloes) are removed, eliminating 14.6% of the original survey area (de Jong et al. 2017).

The photometric redshifts of the sources are measured from co-added

Table 4.1: The names and sizes of the different trough definitions used in this work, including information on the galaxy samples used to select these troughs: the redshift range, the comoving distance range, and the absolute magnitude limits.

Troughs/Galaxies	Trough radius $\theta_{\rm A}$	Redshift range	Distance (h_{70}^{-1}Mpc)	$M_{\rm r}$-limit
Fiducial	$5', 10', 15', 20'$	$0 < z < 0.5$	$0 < D_{\rm c} < 1922.5$	< -19.67
Low redshift	$10'$ $(1.9\, h_{70}^{-1}{\rm Mpc})$	$0.1 < z < 0.198$	$420.0 < D_{\rm c} < 813.9$	< -21.0
High redshift	$6.303'$ $(1.9\, h_{70}^{-1}{\rm Mpc})$	$0.198 < z < 0.3$	$813.9 < D_{\rm c} < 1207.7$	< -21.0

$ugri$ images, which were reduced using the Astro-WISE pipeline (McFarland et al. 2013). From the galaxy colours measured by the Gaussian Aperture and PSF pipeline (GAaP Kuijken et al. 2015), the full redshift probability distribution $n(z_{\rm s})$ of the full source population is calculated, using the direct calibration method described in Hildebrandt et al. (2017). We use this full $n(z_{\rm s})$ for our lensing measurements (as described in Sect. 4.5.2), in order to circumvent the bias inherent in individual photometric source redshift estimates.

4.2.2 GAMA foreground galaxies

One of the galaxy samples we use to define the troughs is obtained using the spectroscopic GAMA survey, which was performed with the AAOmega spectrograph mounted on the Anglo-Australian Telescope. The galaxy locations were selected from the Sloan Digital Sky Survey (SDSS, Abazajian et al. 2009). For this study we use the three equatorial regions (G09, G12 and G15) from the GAMA II data release (Liske et al. 2015), which span a total area of $180\,\deg^2$ on the sky, since these areas are completely overlapping with the KiDS survey. GAMA has a redshift completeness of 98.5% down to Petrosian r-band magnitude $m_{\rm r} = 19.8$, resulting in a catalogue containing $180,960$ galaxies with redshift quality $n_{\rm Q} \geq 2$. As recommended, we only use the galaxies with redshift quality $n_{\rm Q} \geq 3$, which amounts to 99.74% of the full catalogue. In order to indicate regions where the survey is less complete, GAMA provides a 'mask' which contains the redshift completeness of galaxies on a $0.001\,\deg$ Cartesian grid. We use this mask to account for incomplete regions during the trough classification.

To mimic the galaxy sample corresponding to resolved haloes in the MICE-GC mock catalogues (see Sect. 4.2.4), we only use galaxies with absolute r-band magnitude $M_{\rm r} < -19.67$. The GAMA restframe $M_{\rm r}$ is determined by fitting Bruzual and Charlot (2003) stellar population synthesis models to the $ugrizZYJHK$ spectral energy distribution of SDSS and VIKING observations (Abazajian et al. 2009; Edge et al. 2013), and corrected for flux falling outside the automatically selected aperture (Taylor et al. 2011b). Together, the $n_{\rm Q}$ and $M_{\rm r}$ cuts result in a sample of 159,519 galaxies (88.15% of the full catalogue), with a redshift range between $0 < z_{\rm G} < 0.5$ and a mean redshift of $\overline{z_{\rm G}} = 0.24$. The projected number density of this sample of GAMA galaxies, together with their completeness mask, will be used to define the troughs as detailed in Sect. 4.3.1.

4.2.3 KiDS foreground selection

Since the currently available area of the KiDS survey is 2.5 times larger than that of the GAMA survey (and will become even larger in the near future) it can be rewarding to perform both the trough selection and lensing measurement using the KiDS galaxies alone, employing the full $454\,\mathrm{deg}^2$ area of the current KiDS-450 dataset. To be able to compare the KiDS troughs to those obtained using GAMA, we select a sample of KiDS galaxies that resembles the GAMA sample as closely as possible. Because GAMA is a magnitude-limited survey ($m_{\mathrm{r,Petro}} < 19.8$), we need to apply the same magnitude cut to the (much deeper) KiDS survey. Since there are no Petrosian r-band magnitudes available for the KiDS galaxies, we use the KiDS magnitudes that have the most similar m_{r}-distribution: the extinction-corrected and zero-point homogenised isophotal r-band magnitudes (de Jong et al. 2017). These magnitude values, however, are systematically higher than the Petrosian magnitudes from GAMA. We therefore match the KiDS and GAMA galaxies using their sky coordinates, and select the magnitude cut based on the completeness of this match. Using $m_{\mathrm{r,iso}} < 20.2$, the completeness of the match is 99.2%. This cut results in a slightly higher number density than that of real GAMA sample, but this small difference does not significantly affect our results which are primarily based on the relative number density (compared to other apertures or the mean density).

In addition, we cut the KiDS galaxies at the maximum redshift of GAMA: $z_{\mathrm{ANN}} < 0.5$. Contrary to the KiDS source redshifts used for the lensing measurement, where we can use the redshift probability distribution of the full population (see Sect. 4.3.2), the application of this cut and the use of KiDS galaxies as lenses requires individual galaxy redshifts. These photometric redshifts are determined using the machine learning method ANNz2 (Sadeh et al. 2016) as described in Sect. 4.3 of de Jong et al. (2017). Following Bilicki et al. (2017) the photo-z's are trained exclusively on spectroscopic redshifts from the equatorial GAMA fields[2]. This is the first work that uses KiDS photometric redshifts through machine learning to estimate the distances of the lenses. Compared to the spectroscopic GAMA redshifts z_{G}, the mean error $\delta z = (z_{\mathrm{ANN}} - z_{\mathrm{G}})/z_{\mathrm{G}}$ on the ANNz2 photometric redshifts is -3.26×10^{-4}, with a standard deviation of 0.036, much smaller than the width of the redshift selections used in this work (see Sect. 4.5.1). Finally, to mimic the galaxy sample corresponding to resolved haloes in the

[2] Bilicki et al. (2017) use a slightly different apparent magnitude cut to select the GAMA-like galaxy sample: $m_{\mathrm{r,auto}} < 20.3$. However, since this is an a-posteriori cut it does not influence the determination of the photo-z values.

mock catalogues (see Sect. 4.2.4), we apply the absolute r-band magnitude cut $M_{\rm r} < -19.67$. These absolute magnitudes: $M_{\rm r} = m_{\rm r,iso} - D_{\rm M} + K_{\rm cor}$, are determined using distance moduli $D_{\rm M}$ based on the $z_{\rm ANN}$ redshifts. The K-corrections $K_{\rm cor}$ are calculated from the isophotal g- and i-band magnitudes of the KiDS galaxies, using the empirical relation in Table 4 of Beare et al. (2014).

To remove stars from our galaxy sample, we use a star/galaxy separation method based on the source morphology (described in Sect. 4.4 of de Jong et al. 2015). We also mask galaxies that have been affected by readout and diffraction spikes (flag 1 and 4), by saturation cores and primary haloes of bright stars (flag 2 and 8), or by bad pixels (flag 64) in any band (u, g, r or i). We do not remove galaxies affected by secondary and tertiary stellar haloes (flag 16 and 32) because these do not heavily affect bright galaxies, and we do not apply manual masking (flag 128) because it is not yet performed on the two southern DR3 patches (G23 and GS). For more information on the masking flags, see Sect. 4.5 of de Jong et al. (2015). In addition, we remove galaxies that have an unreliable magnitude measurement in any band, as recommended in App. 3.2 of de Jong et al. (2017). Using this selection, we obtain a sample of 309,021 KiDS galaxies that resemble the GAMA and MICE-GC galaxy populations.

Based on the aforementioned image defects, the KiDS survey provides an automatic mask that flags affected pixels. For simplicity we only use the r-band pixel mask, which has a less than 1% difference with the pixel mask based on all bands. We use this map to account for incomplete regions during the trough classification procedure (see Sect. 4.3.1). In order to save computational time, we create a map that provides the survey completeness on a $0.04\,\deg$ Cartesian grid, by calculating the ratio of 'good' pixels (flag 0, 16, 32 and 128) in the square area surrounding each grid point. The grid spacing of the resulting mask is the same as that used for the trough selection, and is chosen such that it is at least two times smaller than the radius of the smallest troughs.

4.2.4 MICE mock galaxies

We wish to apply the same trough detection and analysis to simulated data, in order to compare and interpret our observational results. The MICE-GC N-body simulation presented by Fosalba et al. (2015a) contains $\sim 7\times10^{10}$ DM particles in a $(3072\,h_{70}^{-1}{\rm Mpc})^3$ comoving volume, allowing the construction of an all-sky lightcone with a maximum redshift of $z = 1.4$. From this lightcone Crocce et al. (2015) built a halo and galaxy catalogue, using a Halo Occupation Distribution (HOD) and Halo Abundance Matching (HAM) technique. Its large volume and fine spatial resolution make MICE-GC mocks ideally suited for accurate modelling of both large-scale (linear) and small-scale (non-linear) clustering and structure growth. The mock galaxy clustering as a function of luminosity has been constructed to reproduce observations from SDSS (Zehavi et al. 2011) at lower redshifts ($z < 0.25$), and has been validated against the COSMOS catalogue (Ilbert et al. 2009) at higher redshifts ($0.45 < z < 1.1$). The MICE-GC catalogue resolves DM halos down to a mass of $\sim 10^{11}\ h_{70}^{-1}\mathrm{M}_{\odot}$, corresponding to galaxies with an absolute magnitude < -18.9. Since this absolute magnitude includes a cosmology correction such that: $M_{\mathrm{r,MICE}} = M_{\mathrm{r}} - 5\log_{10}(h = 0.7)$, we apply an $M_{\mathrm{r}} < -18.9 - 0.77 = -19.67$ cut to the KiDS and GAMA samples in order to resemble the mock galaxy population.

From the MICE-GC catalogue, which is publicly available through `http://cosmohub.pic.es`, we obtain the sky coordinates, redshifts, comoving distances, absolute magnitudes and SDSS apparent magnitudes of the mock galaxies. In order to create a GAMA-like mock galaxy sample, we limit the MICE redshifts to $z < 0.5$. When considering the choice of magnitude cut, we find that the distribution of the SDSS magnitudes in the MICE catalog is very similar to that of the isophotal KiDS magnitudes. We therefore limit the MICE galaxies to $m_{\mathrm{r}} < 20.2$, and find that indeed the galaxy number density of the GAMA-like KiDS and MICE samples are almost equal (see Fig. 4.1 in Sec. 4.3.1). Like the GAMA galaxies and the GAMA-like KiDS sample, this sample of MICE foreground galaxies is used to define troughs following the classification method described in Sect. 4.3.1.

Each galaxy in the lightcone also carries the lensing shear values γ_1 and γ_2 (with respect to the Cartesian coordinate system) which were calculated from the all-sky weak lensing maps constructed by Fosalba et al. (2015b), following the 'onion shell' method presented in Fosalba et al. (2008). In this approach the DM lightcone is decomposed and projected into concentric spherical shells around the observer, each with a redshift width of $\mathrm{d}z \approx 0.003(1+z)$. These 2D DM density maps are multiplied by the appropriate lensing weights and combined in order to derive the galaxies' lensing properties. The results agree with the more computationally expensive 'ray-tracing' technique within the Born approximation. We will use these shear values (in the same way we used the ellipticities observed by KiDS) to obtain mock lensing profiles around troughs, following the weak lensing method described in Sect. 4.3.2. To this end we create a MICE background source sample with $0.1 < z < 0.9$ and $m_{\mathrm{r}} > 20$, the same redshift and apparent magnitude cuts as applied to the KiDS background sources (Hildebrandt et al. 2017). Also, in order to resemble the KiDS redshift distribution more closely, we choose to apply an absolute magnitude cut of $M_{\mathrm{r}} > -19.3$ on the mock galaxies. Note that any cut on the mock galaxy sample does not affect the shear values (which do not depend on any mock galaxy property) but only the redshift distribution of the sources, which is used in Sect. 4.5.2 to calculate the Excess Surface Density profiles.

Because all quantities in the mock catalogue are exactly known, we do not need to take into account measurement errors into the calculation of the mock lensing signals. However, there do exist differences between measurements from different parts of the sky caused by sample variance, and possibly by underlying large-scale density fluctuations (cosmic variance, Somerville et al. 2004). To obtain an estimate of these uncertainties we use the full MICE-GC public lightcone, which has an area of $90^{\circ} \times 90^{\circ}$. We divide this area into 16 patches of $20^{\circ} \times 20^{\circ} = 400\,\mathrm{deg}^2$, each spanning approximately the same size as the used KiDS area. One of these patches is used as our fiducial mock galaxy sample. Comparing the results obtained from the fiducial patch with those of the 15 other galaxy samples, provides an estimate of the sample and cosmic variance within the mocks. As MICE has no mask to indicate unreliable survey areas, we create an artificial mask for each $20^{\circ} \times 20^{\circ}$ area, which indicates that the patch is 100% complete and is only used to to indicate its borders.

4.3 Data analysis

The two most important aspects of the data analysis are the classification of the troughs, and the subsequent measurement of their gravitational lensing profiles. For the classification we compare using GAMA galaxies to using the GAMA-like KiDS sample (see 4.2.3). For the measurement of the gravitational lensing effect around these troughs, we use the shapes and photometric redshifts of the KiDS background galaxies. In this section we will discuss the trough classification and lensing measurement methods in detail.

4.3.1 Trough classification

Our approach to trough detection is mainly inspired by the method devised by G16. This effectively comprises measuring the projected number density of galaxies within circular apertures on the sky, and finding the apertures with the lowest galaxy density. Following this method, we define a finely spaced Cartesian grid of positions on the sky. Around each sky position x, we count the number of galaxies within a circular aperture of chosen radius θ_{A}. We perform this method for apertures with different projected radii: $\theta_{\mathrm{A}} = \{5, 10, 15, 20\}$ arcmin, which allows us to study cosmic structure at different scales. To make sure that no information is lost through under-sampling, we choose a grid spacing of $0.04\,\mathrm{deg}$ ($= 2.4\,\mathrm{arcmin}$) which is smaller than $\theta_{\mathrm{A}}/2$, even for the smallest aperture size. Although this spacing is much larger than that used by G16 ($0.86\,\mathrm{arcmin}$), we still need to cope with the significant overlap between neighbouring troughs. Performing tests with reduced overlap between the circles does not significantly change our results, primarily because the key part of the trough lensing profiles is situated outside the trough radius (such that overlap within the circle is not particularly worse than overlap outside the circle). We account for this overlap by ensuring that: 1) the covariance between the lensing profiles of neighbouring troughs is accounted for in the calculation of the error bars (see Sect. 4.3.2), and 2) the same overlap is embedded in the mock trough selection in the MICE simulations, which we use to interpret our results.

The projected galaxy number density $n_{\mathrm{g}}(x, \theta_{\mathrm{A}})$ of each aperture is defined as the galaxy count within radial separation θ_{A} of the sky position x, divided by the unmasked area of the corresponding circle on the sky, determined using the appropriate (KiDS, GAMA or MICE) mask. Each mask provides the survey area completeness on a finely spaced grid, which we average to a $0.04\,\mathrm{deg}$ Cartesian grid to save computational time. We measure the total area completeness for the circle around each grid point, and (following G16) exclude those circles that are less than 80% complete from our sample. We verified that this specific choice of completeness threshold does not significantly affect our results.

The histogram in Fig. 4.1 shows the normalized KiDS and MICE galaxy number density distributions (represented by steps and smooth lines respectively) for apertures with different radii θ_{A}. The density roughly follows a log-normal distribution, as was originally modeled by Coles and Jones (1991), but with a slight deviation from the mean density. This effect is larger for circles with a smaller area, which is expected since larger apertures measure the average density over a larger area. The deviation tends more towards higher densities than lower, because the galaxy density can never reach values below 0. This leads to an increasingly skewed density distribution for smaller apertures, which is visible in both observa-

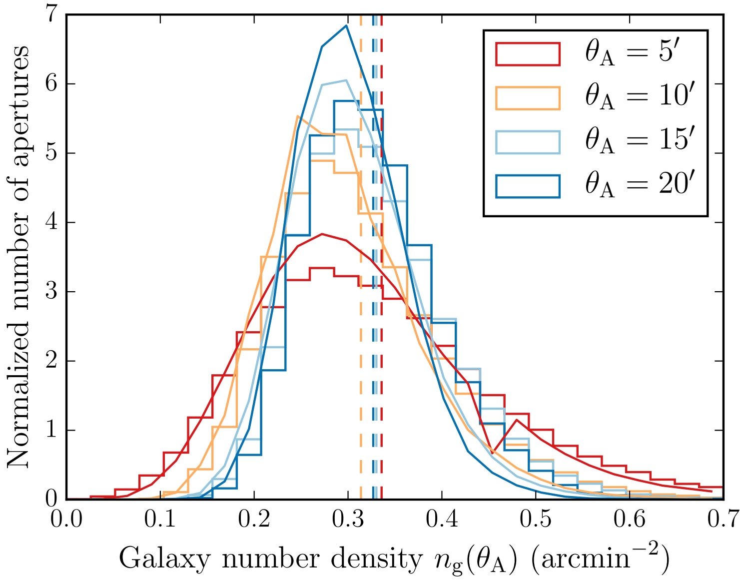

Figure 4.1: This histogram shows the distribution of the normalized number density $n_{\rm g}$ of the KiDS (steps) and MICE (lines) galaxies used to define the troughs, inside all used apertures (those with an effective area $> 80\%$). The colours designate apertures of different radius $\theta_{\rm A}$. As expected, the density distribution of circles with a smaller area is more asymmetric, and has a larger deviation from the mean density $\overline{n_{\rm g}}(\theta_{\rm A})$ (dashed lines). The 'troughs' are defined as all underdense apertures (i.e. $n_{\rm g} < \overline{n_{\rm g}}(\theta_{\rm A})$), while all overdense apertures (i.e. $n_{\rm g} > \overline{n_{\rm g}}(\theta_{\rm A})$) are called 'ridges'.

tional and mock data. We verified that this skewness is also observed in the density distribution of troughs selected using GAMA galaxies.

Following G16 we determine, for each of these circles, the proportion $P(x, \theta_{\rm A})$ of equally sized apertures that have a lower galaxy density than the circle considered. Arranging the apertures in this way means that low-density circles will have a low value of P (down to $P = 0$), while high-density circles will have a high P-value (up to $P = 1$). A circle containing the median density will have $P = 0.5$. In the fiducial definition of G16, all apertures in the lower quintile (20%) of galaxy density (i.e. $P(x, \theta_{\rm A}) < 0.2$) are called troughs, while apertures in the higher quintile (i.e. $P(x, \theta_{\rm A}) > 0.8$) are considered overdensities (which we will hereafter call 'ridges').

We will use the terms 'trough' and 'ridges' more generally, based on the overdensity $\delta(x, \theta_{\rm A})$ with respect to the mean galaxy number density $\overline{n_{\rm g}}$ of the total effective area of the survey. The overdensity is defined as:

$$\delta(x, \theta_{\rm A}) = \frac{n_{\rm g}(x, \theta_{\rm A}) - \overline{n_{\rm g}}(\theta_{\rm A})}{\overline{n_{\rm g}}(\theta_{\rm A})} \,. \quad (4.1)$$

In our classification, all underdense apertures (i.e. $\delta(x, \theta_{\rm A}) < 0$) are called troughs, while all overdense apertures are called ridges. This definition does not *a priori* exclude any apertures from our combined sample of troughs and ridges, allowing us to take advantage of all available data. We will further specify sub-samples of troughs and ridges, selected as a function of both P and δ, where necessary throughout the work.

4.3.2 Lensing measurement

In order to measure the projected mass density of the selected troughs and ridges, we use weak gravitational lensing (see Bartelmann and Schneider 2001; Schneider et al. 2006, for a general introduction). This method measures the coherent deflection of light from many background galaxies (sources) by foreground mass distributions (lenses). This gravitational deflection causes a distortion in the observed shapes of the source images of $\sim 1\%$, which can only be measured statistically. This is done by averaging, from many background sources, the projected ellipticity component $\epsilon_{\rm t}$ tangential to the direction towards the centre of the lens, which is equal to the 'tangential shear' $\gamma_{\rm t}$. This quantity is averaged within circular annuli around the center of the lens, to create a shear profile $\gamma_{\rm t}(\theta)$ as a function of the separation angle θ to the lens centre. For each annulus, $\gamma_{\rm t}(\theta)$ is a measure of the density contrast of the foreground mass distribution. In order to obtain a reasonable signal to noise ratio (S/N), the shear measurement around many lenses is 'stacked' to create the average shear profile of a specified lens sample. In this work, the centres of the lenses are the grid points that define our circular troughs and ridges (as defined in Sect. 4.3.1).

The background sources used to measure the lensing effect are the KiDS galaxies described in Sect. 4.2.1. Following Hildebrandt et al. (2017), we only use sources with a best-fit photometric redshift $0.1 < z_{\rm B} < 0.9$. For troughs defined at a specific redshift we only select sources situated beyond the troughs, including a redshift buffer of $\Delta z = 0.2$ (see Sect. 4.5.2). This cut is not applied when troughs are selected over the full redshift range. This can allow sources that reside at similar redshifts as the lenses to be used in the measurement, possibly resulting in a contamination of the lensing signal by sources that are intrinsically aligned with the troughs. However, most low-redshift sources have already been removed by the $m_{\rm r} > 20$

cut (Hildebrandt et al. 2017). Also, the intrinsic alignment effect primarily plays a role in very high density regions, on small ($\lesssim 1\,h_{70}^{-1}\mathrm{Mpc}$) scales. On the large scales probed by the troughs, the effect of intrinsic alignment is at most a few percent, especially since only relatively light (i.e. faint) KiDS galaxies are considered (Heymans et al. 2006b; Blazek et al. 2012). The small effect from intrinsic alignment that remains is also present in the results obtained from the MICE mock catalogue, to which we compare our observations.

The ellipticities of the source galaxies are measured using the self-calibrating *lens*fit pipeline (Miller et al. 2007, 2013b; Fenech Conti et al. 2017). For each galaxy this Bayesian model fitting method also produces the *lens*fit weight w, which is a measure of the precision of the shear estimate it provides. We would like to give more weight to the contribution of sources with a more reliable ellipticity measurement, and therefore incorporate the *lens*fit weight of each source into our combined shear measurement as follows:

$$\overline{\gamma} = \frac{1}{1+\mu} \frac{\sum_{ls} w_s \, \epsilon_{\mathrm{t},ls}}{\sum_s w_s} \,, \tag{4.2}$$

where the sum goes over each lens l and source s, and the factor $1+\mu$ is used to correct for 'multiplicative bias'. Fenech Conti et al. (2017) showed, based on extensive image simulations, that shears are biased at the $1-2\%$ level, and how to correct for this using a multiplicative bias correction m for every ellipticity measurement. Following Dvornik et al. (2017), the value of μ is calculated from the m-corrections in 8 redshift bins (with a width of 0.1) between $0.1 < z_{\mathrm{B}} < 0.9$. The average correction in each bin is defined as follows:

$$\mu = \frac{\sum_s w_s m_s}{\sum_{ls} w_s} \,. \tag{4.3}$$

The required correction is small ($\mu \approx 0.014$) independent of radial distance, and reduces the residual multiplicative bias to $\lesssim 1\%$. The errors on our shear measurement are estimated by the square-root of the diagonal of the analytical covariance matrix, as described in Sect. 3.4 of Viola et al. (2015). The covariance matrix of the lensing signal is based on the contribution of each individual source, and take into account the covariance of sources that contribute to the shear profile of multiple lenses.

In addition to measuring the lensing profile around troughs and ridges, we stack the shear around *all* grid points. This 'random signal' γ_0 does not contain a coherent shear profile, but only systematic effects resulting from the imperfect correction for the PSF anisotropy in combination with the survey edges and masks. In accordance with the real trough measurements, the apertures with an effective area less than 80% of the total circle area are removed (see Sect. 4.3.1). When using the GAMA survey area and masks, the random signal is consistent with 0 within the error bars, up to radius $\theta = 70\,\mathrm{arcmin}$ where it rises to $\gamma_0 \sim 3 \times 10^{-3}$ for all values of θ_A, while the KiDS random signal already starts to deviate at $\theta \approx 20\,\mathrm{arcmin}$ (see Sect. 4.4.1). To correct for this effect at larger scales, we subtract the appropriate γ_0 from all lensing measurements. Given this result, and our grid spacing of $0.04\,\mathrm{deg} = 2.4\,\mathrm{arcmin}$ (see Sect. 4.3.1), we compute our lensing profiles for 20 logarithmically spaced bins within the range $2 < \theta < 100\,\mathrm{arcmin}$.

4.4 Trough shear profiles

After a general classification of the troughs and ridges we define more specific samples, dedicated to obtaining specific observables from their measured lensing profiles. First, we compare the trough shear profiles of the KiDS- vs. GAMA-selected troughs, to decide on the best trough sample. Using these troughs, we measure the shear amplitude of the lensing profiles as a function of their density percentile $P(x, \theta_\mathrm{A})$, for apertures of different sizes θ_A. This allows us to study non-linearities in cosmic structure formation, and to define an optimal way to stack the shear signals of troughs/ridges in order to optimize the S/N.

4.4.1 KiDS vs. GAMA troughs

The very complete and pure sample of GAMA galaxies allows us to define a clean sample of troughs. However, since the currently available area of the KiDS survey is 2.5 times larger than that of the GAMA survey, we also use a set-up that uses the KiDS galaxies to define the troughs. We select both trough samples following the same classification method (see Sect. 4.3.1), using either the real GAMA galaxies (described in Sect. 4.2.2) or the GAMA-like KiDS sample (defined in Sect. 4.2.3) as our trough-defining galaxies. We use the corresponding completeness mask of the KiDS/GAMA survey to remove unreliable troughs (i.e. with an area $< 80\%$ complete).

To correct for systematic effects, the appropriate random shear profile γ_0 (defined in Sect. 4.3.2) is subtracted from the trough lensing profiles. The random signals for KiDS and GAMA are shown in Fig. 4.2. When using the GAMA survey area and mask, γ_0 is consistent with 0 (within 1σ error bars) up to $\theta = 70\,\mathrm{arcmin}$ and slightly positive beyond. When using the

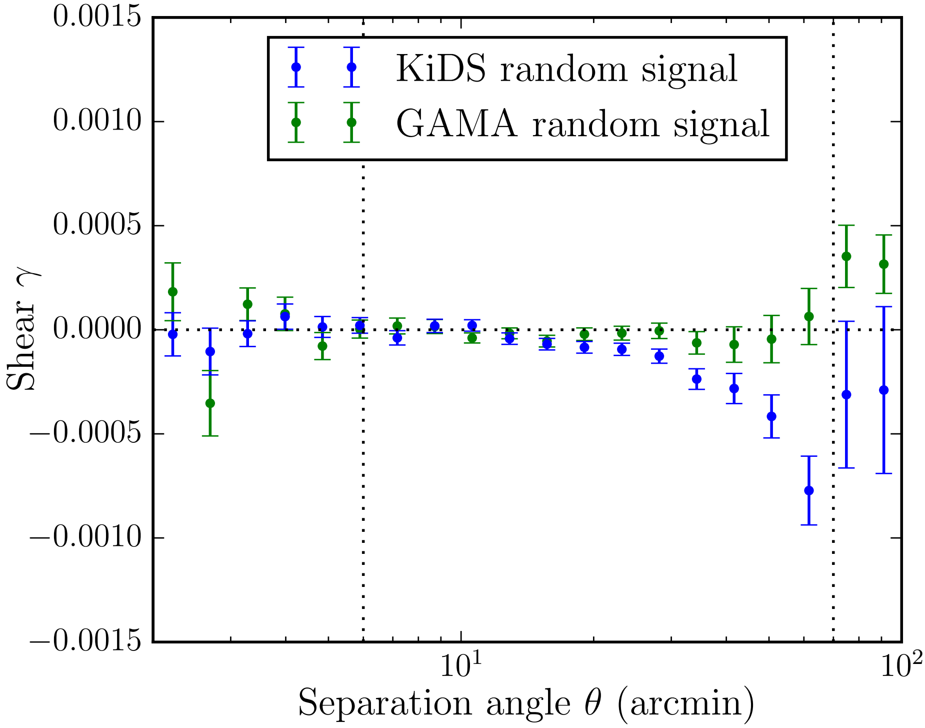

Figure 4.2: The random shear profile γ_0 (including 1σ analytical covariance errors) as a function of separation angle θ, which results from stacking *all* used apertures with an area $> 80\%$ complete. Using the GAMA area and mask, the systematic effects are consistent with 0 up to $\theta = 70\,\mathrm{arcmin}$, while the KiDS random signal already starts to deviate at $\theta \approx 20\,\mathrm{arcmin}$ as a result of the patchy survey area of KiDS outside the GAMA overlap.

KiDS survey area and mask, γ_0 is only consistent with 0 up to $\theta \approx 20\,\mathrm{arcmin}$ and increasingly negative beyond. This difference does not significantly depend on the choice of area completeness threshold, and also occurs when we apply no completeness mask at all. However, when we perform the γ_0 measurement using the KiDS mask on the GAMA area only, the systematic effect is significantly reduced. This shows that the difference between the random signals is primarily caused by the patchy surface of the KiDS-450 dataset beyond the GAMA area (see e.g. Fig. 1 of Hildebrandt et al. 2017).

The main goal of this exercise, however, is to find which galaxy sample provides the best results, i.e. trough lensing profiles with the highest S/N. For this initial test, we use the fiducial trough definition of G16: the apertures with the lowest 20% in density percentile (i.e. $P(\theta_{\mathrm{A}}) < 0.2$).

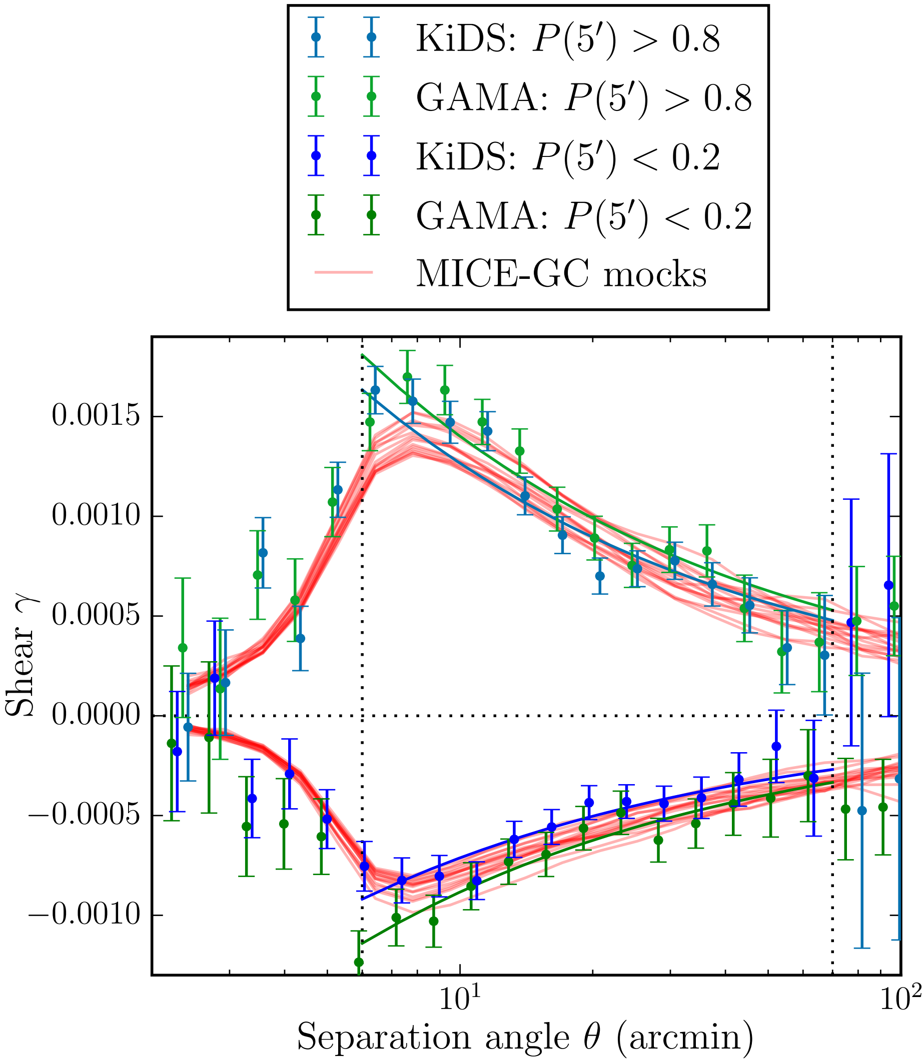

Figure 4.3: The gravitational shear profile $\gamma(\theta)$ (with 1σ errors) resulting from KiDS (blue points) and GAMA (green points) troughs and ridges, including a comparison with the MICE-GC mock troughs from 16 independent patches (red lines). All troughs and ridges have a radius $\theta_{\mathrm{A}} = 5\,\mathrm{arcmin}$, and are selected following the fiducial G16 definition. A simple $A/\sqrt{\theta}$ function (solid blue/green lines) is used to determine the best-fit amplitude A of the KiDS and GAMA troughs.

In Fig. 4.3 we show the stacked shear profiles $\gamma(\theta)$ of troughs with radius $\theta_{\mathrm{A}} = 5\,\mathrm{arcmin}$, selected using the KiDS or GAMA galaxies. For comparison we also include the trough shear profiles obtained using all 16 patches of the MICE mock catalogue, where the vertical spread in the 16 profiles gives an estimate of the sample and cosmic variance. The GAMA-selected troughs have a slightly deeper shear profile than the KiDS-selected troughs, but within the 1σ analytical covariance errors both profiles agree with the predictions from the MICE-GC simulation. However, when we use the KiDS galaxies to select troughs but restrict the used area to the GAMA equatorial fields, we find that the KiDS trough profiles are of equal depth as those from GAMA. This suggests that, like the systematic effects measured by the randoms, the shallower trough lensing profile is caused by the patchy survey area of KiDS. This patchy area reduces the completeness of the circles, which diminishes the accuracy of the density measurements and results in shallower shear profiles.

The dotted vertical lines indicate the radial separation range: $1.2\,\theta_{\mathrm{A}} < \theta < 70\,\mathrm{arcmin}$, that is sensitive to the shear signal from troughs. The reason for this is that: 1) inside θ_{A} the lensing is not sensitive to the full trough mass (where we leave a 20% buffer outside the trough edge), and 2) the lensing signal is very sensitive to systematic effects outside $\theta = 70\,\mathrm{arcmin}$. Within this radial range, we observe that both the trough and ridge shear signals closely follow a power law. For the positive lensing signal around overdense ridges this is expected, since the lensing profiles around galaxies and clusters can generally be described with the negative power law (with a slope of -0.8) resulting from a Navarro-Frenk-White profile (NFW, Navarro et al. 1996) plus two-halo term (see e.g. Fig. 5 of van Uitert et al. 2011). Fig. 4.3 shows that both the ridges and the troughs follow an approximate power law shape. We can therefore fit a simple power law $\gamma(\theta) = A\,\theta^{\alpha}$ within the specified radial range, to obtain the best-fit amplitude A and index α of the lensing signal. Because we are mainly interested in the amplitude, we fix the value of α with the help of the MICE-GC simulations. By fitting the power law (with both A and α as free parameters) to all 16 fiducial MICE trough lensing signals, we find a mean best-fit index value $\overline{\alpha}$ of -0.45 for troughs and -0.55 for ridges. We therefore choose to fit all trough lensing profiles in this work with the function: $\gamma(\theta) = A/\sqrt{\theta}$. However, we verified that our conclusions do not significantly depend on the specific choice of α, by performing the same analysis with $\alpha = -1$ and finding similar results.

From the best-fit amplitudes thus obtained, we wish to find a measure of the signal to noise ratio S/N in order to select the best troughs. We define the S/N as: $A/\delta A$, where δA is the 1σ error on the best-fit amplitude, based on the full analytical covariance matrix of the shear profile. Using this definition, we find that the GAMA troughs are detected with a significance of $|S/N| = 12.0$, while the KiDS troughs have $|S/N| = 12.3$. So, although the GAMA troughs are slightly deeper, the shear measurements of KiDS compensate for this by having smaller error bars, as expected from the larger survey area. The conclusion of this initial comparison is that, regarding trough lensing studies, the current patchy KiDS area already outperforms the highly complete and contiguous GAMA survey. We will therefore use the KiDS survey to select the troughs and ridges studied within this work, but we verify for each measurement that the same results are obtained using the GAMA galaxies.

4.4.2 Lensing amplitudes

After this initial test, which uses only the deepest (highest) 20% of the troughs (ridges), we wish to study all troughs and ridges as a function of their density percentile $P(\theta_{\rm A})$. Considering apertures of fixed radius $\theta_{\rm A}$ we divide them into 20 samples of increasing percentile value, using a bin width of $\mathrm{d}P = 0.05$. We measure the shear profile $\gamma(\theta)$ (using the method described in Sect. 4.3.2) for the apertures in every percentile bin. Figure 4.4 shows the KiDS and MICE lensing profiles in the 20 percentile bins, for circles with radius $\theta_{\rm A} = 5\,\mathrm{arcmin}$. To each shear measurement we fit the same function, $\gamma(\theta) = A/\sqrt{\theta}$, within the appropriate radial range (see Sect. 4.4.1). As expected the apertures with low P-values correspond to the deepest troughs, resulting in a negative shear signal starting at the trough edge (in this case at $\theta > 5\,\mathrm{arcmin}$). In contrast, the circles with high P-values show a strong positive shear signal beyond the edge of the ridge. It is already apparent that troughs and ridges are not symmetrical, but that the lensing signal is stronger for the highest ridges than for the deepest troughs. This is an indication that the skewness of the galaxy number density distribution (seen in Fig. 4.1) is reflected by the total (baryonic + DM) density distribution. This skewness is not only indicated by most extreme densities, but also by those close to the median. Examining these, we find that the turning point between negative and positive lensing amplitudes is *not* situated at the median density ($P = 0.5$). This can be better appreciated from the left panel of Fig. 4.5, which shows the best-fit A as a function of P for apertures of different radius $\theta_{\rm A}$. For both the KiDS and MICE data the turning point $A = 0$ is not reached at $P = 0.5$, but at $P \approx 0.55 - 0.6$.

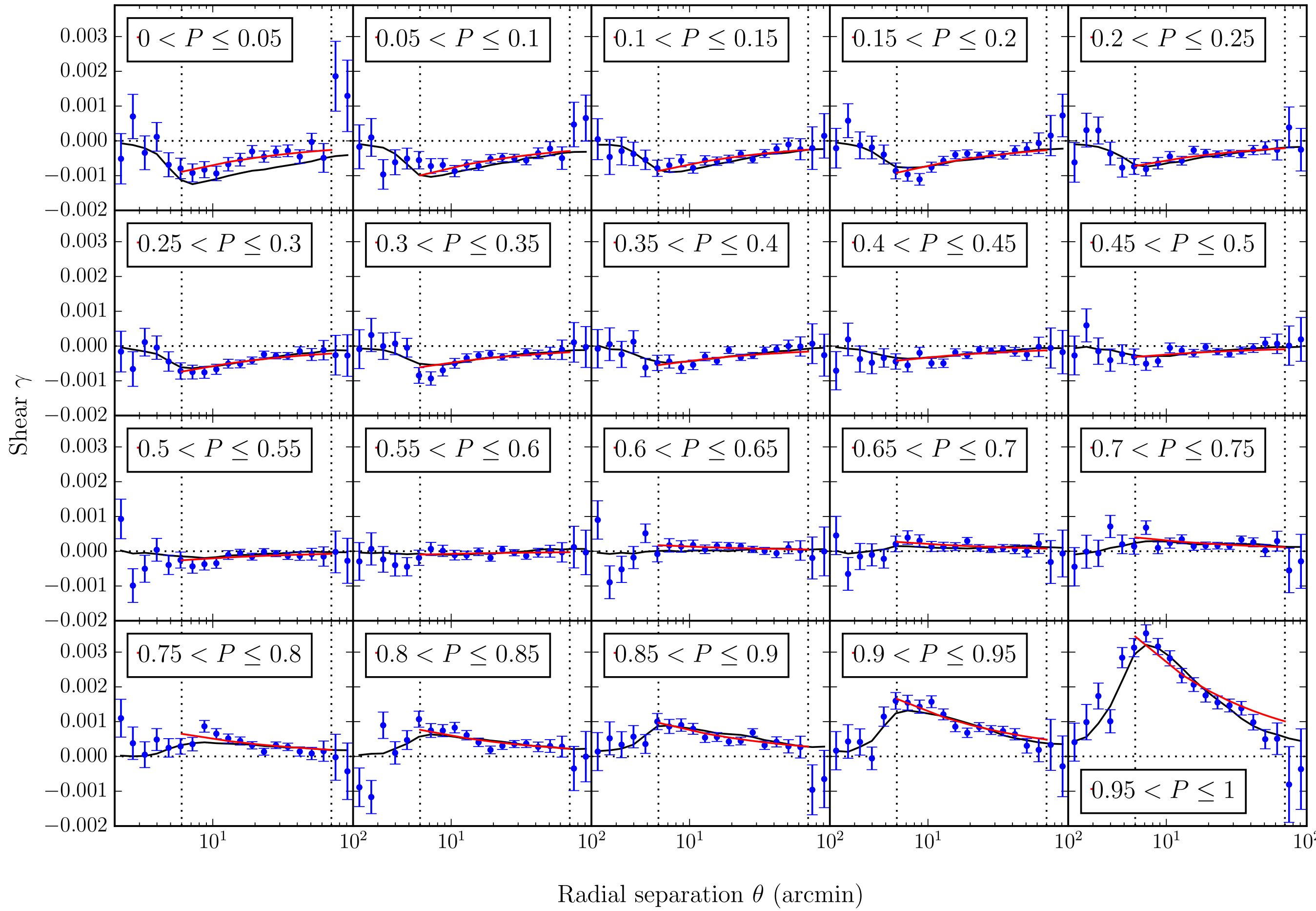

Figure 4.4: Each panel shows the KiDS (blue dots with 1σ errors) and MICE (black line) shear profiles $\gamma(\theta)$, resulting from apertures of size $\theta_A = 5\,\mathrm{arcmin}$. The shear profile of these apertures is stacked in 20 bins of increasing density percentile $P(x, \theta_A = 5)$. For underdense apertures (troughs) the amplitude A of the lensing signal becomes negative outside the trough radius, while for overdense apertures (ridges) A becomes positive. A simple power law fit: $A/\sqrt{\theta}$ (red line), within the fitting range (dotted vertical lines) is used to obtain A as a function of P.

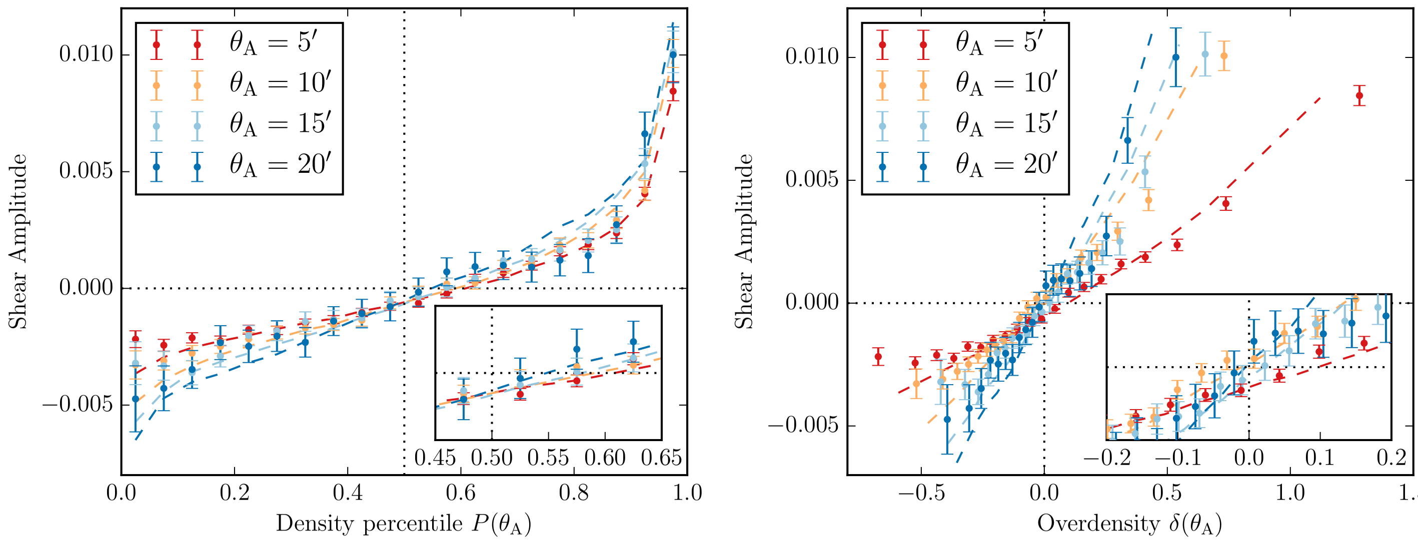

Figure 4.5: The amplitude A of the KiDS (points with 1σ errors) and MICE (dashed lines) shear signals as a function of the density percentile P (left) and overdensity δ (right), for apertures of different angular radius θ_A. The turning point between negative and positive A situated at at the mean density ($\delta = 0$) as is expected when there is only linear galaxy bias, except when $\theta_A = 5'$. This turning point, however, is not situated at the median density ($P = 0.5$) but at $P \approx 0.55 - 0.6$, which means that the density distribution is skewed. The smallest apertures also reveal the skewness of the density distribution, since their distribution extends to more extreme values of P, δ and A for the ridges than for the troughs, while larger apertures have a more symmetrical $A(\delta)$ distribution.

The right panel of Fig. 4.5 shows A as a function of the overdensity $\delta(\theta_{\rm A})$, which is defined in Eq. 4.1, for both KiDS and MICE troughs/ridges. The δ-value of each bin is taken to be the mean overdensity $\overline{\delta}(\theta_{\rm A})$ of all apertures in each percentile bin. For all aperture sizes the $A(\delta)$ relation is approximately linear, with the turning point between negative and positive A situated at the mean density ($\delta = 0$). This is expected when there is only linear galaxy bias, i.e.: there exists a linear relation between galaxies and DM. Only the smallest apertures, $\theta_{\rm A} = 5\,{\rm arcmin}$, seem to show a slight trace of non-linear galaxy bias near the centre, in both the observational and the mock data. This could be explained by the fact that non-linearities in the density field are more prevalent at smaller scales. Furthermore, the discrepancy between the $A(P)$ and $A(\delta)$ relations shows that (like the galaxy number density distribution in Fig. 4.1) the mass distribution measured using lensing is skewed. This asymmetry is caused by the fact that, during cosmic structure formation through clustering, the density of matter is bound to a strict lower limit (a completely empty region) but not to an upper limit. This is also revealed by the asymmetry between the lensing amplitudes at the lowest and highest P and δ. For smaller apertures, the positive amplitudes are significantly larger than the negative amplitudes. This effect is less pronounced for the largest apertures, which have more symmetrical $A(\delta)$ relations. These non-linearities can in principle be used as a statistic to constrain cosmological parameters, analogous to performing shear peak statistics (Dietrich and Hartlap 2010; Liu et al. 2015; Kacprzak et al. 2016).

4.4.3 Optimal trough weighting

Instead of selecting troughs and ridges using a 'hard cut' in the percentile $P(x, \theta_{\rm A})$ of the apertures, one can apply a more sophisticated weighting scheme to stack the shear signals of the apertures. In order to obtain the most significant lensing detection, the optimal weighting should be based on the S/N of the contribution from each trough (or ridge) to the lensing signal (where we define the S/N as $A/\delta A$, see Sect. 4.4.1). The resulting S/N as a function of percentile P is shown in Fig. 4.6. In this relation the peaks at very high and low P are reduced compared to those in the $A(P)$ relation, since very low density troughs (and very high density ridges) tend to cluster at the centres of large voids (or large clusters). This increases the covariance between the lensing signals of the very deep troughs (or high ridges), thereby increasing the error values. Another noteworthy difference is that the smallest apertures have the highest S/N, while they have the smallest amplitude. The reason for this, is that the number of data-points

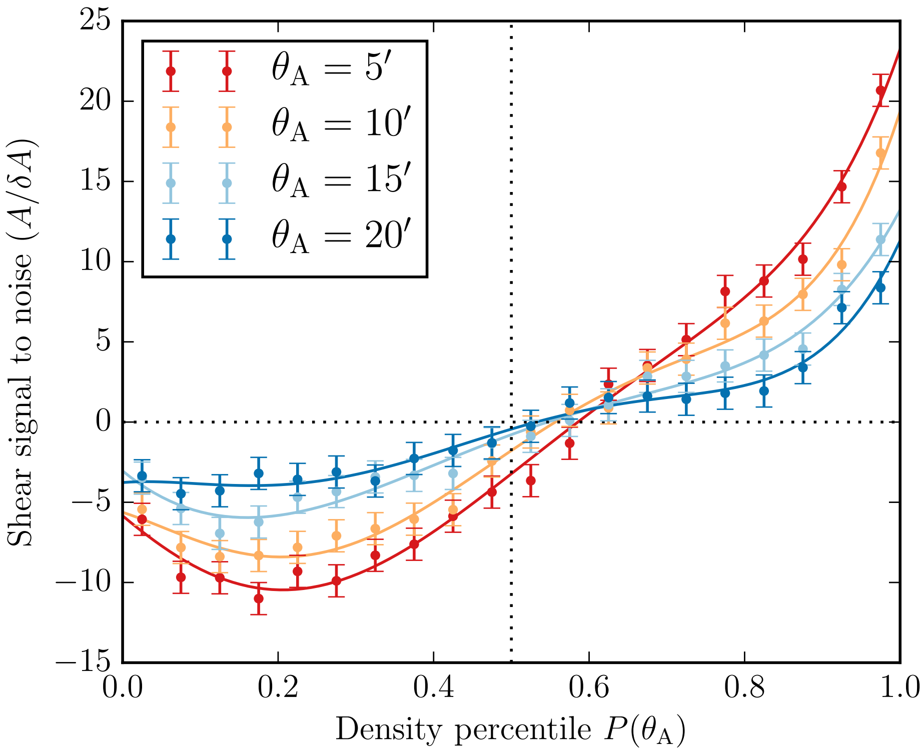

Figure 4.6: The signal to noise ratio, defined as $A/\delta A$, of the KiDS shear profiles as a function of the density percentile P. To obtain the optimal weight to stack the troughs and ridges, we fit a standard $5^{\rm th}$-order polynomial (solid lines) to the measured $A/\delta A$ values (points with 1σ error bars). The resulting weight function $w(P)$ allows us to obtain a (positive) stacking weight $w_{\rm P} = |w(P)|$ for each individual lens.

inside the fitting range ($1.2\,\theta_{\rm A} < \theta < 70\,{\rm arcmin}$) is larger for lower values of $\theta_{\rm A}$. In the end this effect is of no consequence, since only the relative difference in S/N between apertures of the same size are factored into the weighting scheme.

We fit a $5^{\rm th}$-order polynomial to the $A/\delta A$ values in order to find a weight function $w(P)$ that provides a lens weight $w_{\rm P}$ for every individual aperture. We define the weight as the absolute value of this function: $w_{\rm P} = |w(P)|$, in order to obtain a positive weight for both ridges and troughs. Finally, when we compute the combined lensing profile of all troughs or ridges, we use these weights to scale the contribution of each lens to the combined shear signal. The $w_{\rm P}$-value of each lens l is incorporated into

Eq. (4.2), such that it becomes:

$$\overline{\gamma}_{\rm P} = \frac{1}{1+K_{\rm P}} \frac{\sum_l \left(w_{{\rm P},l} \sum_s w_s \epsilon_{\rm t} \right)}{\sum_l \left(w_{{\rm P},l} \sum_s w_s \right)} \, . \tag{4.4}$$

In this way we give higher weights to troughs/ridges that provide a higher S/N, which thus contribute more heavily to the combined shear signal. These same weights are also applied to the average multiplicative bias correction from Eq. (4.3):

$$K_P = \frac{\sum_l \left(w_{{\rm P},l} \sum_s w_s m_s \right)}{\sum_l \left(w_{{\rm P},l} \sum_s w_s \right)} \, . \tag{4.5}$$

Likewise, the lens weight is incorporated into the uncertainty through the calculation of the analytical covariance matrix (see Sect. 4.2.1).

We combine all troughs (ridges) into a single negative (positive) shear signal using the weighting scheme described above. The optimally combined KiDS and MICE lensing profiles are shown in Fig. 4.7, for different aperture sizes $\theta_{\rm A}$. It is clear that the shear signal decreases for troughs/ridges with larger apertures, because the lensing effect is stronger when light passes more closely to the centre of the lens. For the KiDS-selected troughs and ridges, this method results in a $|S/N| = \{17.1, 14.8, 10.0, 7.6\}$ detection of troughs with a size of $\theta_{\rm A} = \{5, 10, 15, 20\}$ arcmin respectively, and a $|S/N| = \{23.6, 19.9, 13.7, 11.0\}$ detection of ridges of the same size. As a comparison, the fiducial stack of troughs with the lowest 20% in density percentile P would result in a $|S/N| = \{12.3, 10.7, 8.4, 5.7\}$ detection trough detection using the same dataset.

To allow for easier visual comparison between the shape of trough and ridge profiles, we include the trough lensing signal with its sign flipped (i.e. $-\gamma_{\rm t}(R)$) in Fig. 4.7. We find that, for all aperture sizes, the shear resulting from ridges is stronger than that from troughs, which again indicates skewness in the total density distribution. Like G16, we observe that the difference between troughs and ridges is slightly increased for the smallest apertures. This can be explained by the fact that non-linearities affect the density field more strongly at smaller scales.

4.5 Redshift evolution

So far we have studied troughs which extend across the entire redshift range of the GAMA galaxies ($0 < z < 0.5$). We can, however, define troughs that

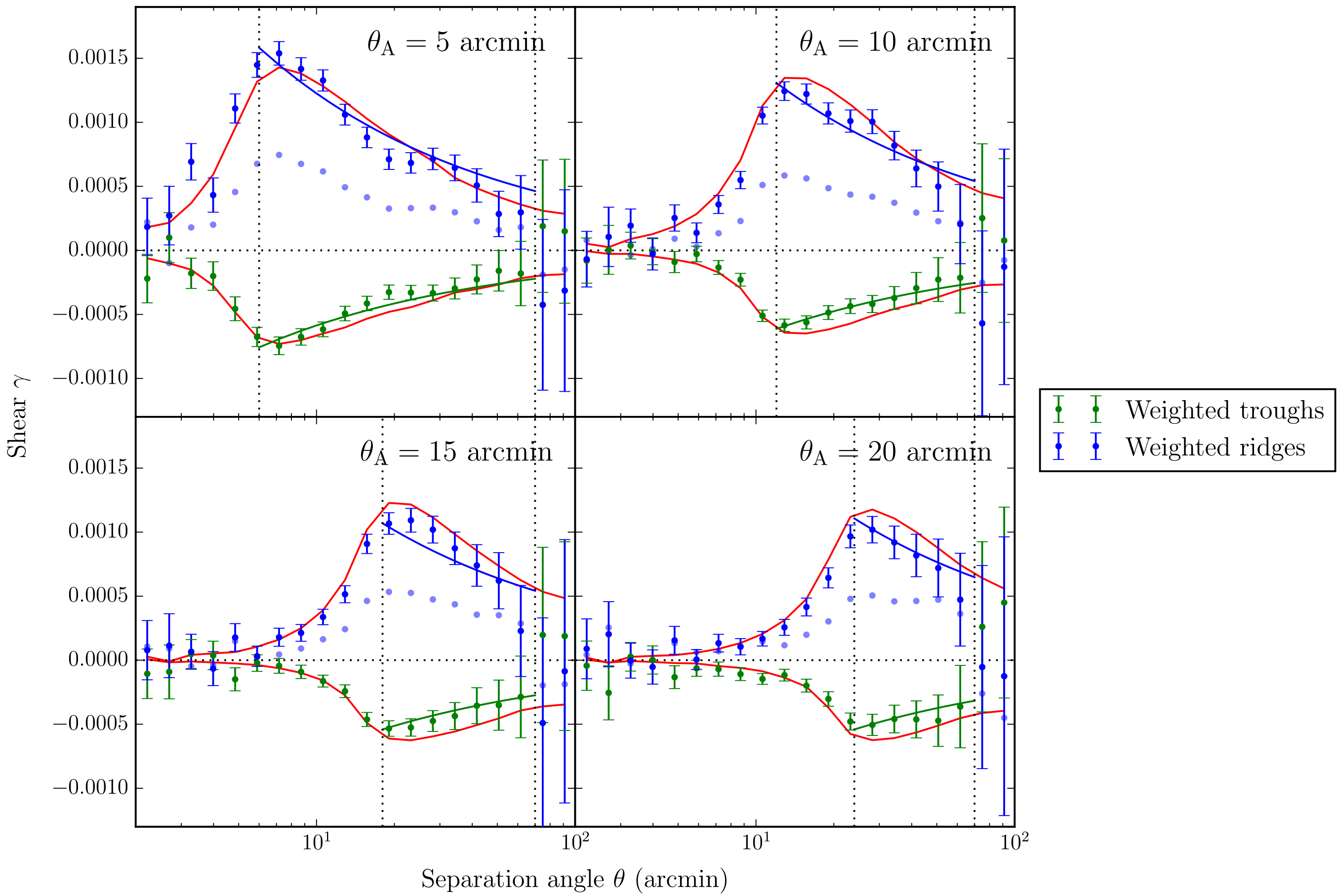

Figure 4.7: The optimally weighted KiDS (dots with 1σ errors) and MICE shear profiles $\gamma(\theta)$ of troughs (green) and ridges (blue), for apertures of increasing radius θ_A. The mirror image of each trough profile (light blue dots) is added to allow for a better visual comparison. We fit a simple power law: $A/\sqrt{\theta}$ (blue/green lines), within the fitting range (dotted vertical lines) to obtain the amplitude A of the lensing signals. For all aperture sizes, the shear from overdensities (ridges) is stronger than that of underdensities (troughs). This difference, which signifies non-linearities in the density field, is slightly larger for the smallest apertures.

cover only a part of this range, which allows us to study the evolution of troughs and ridges over cosmic time. In this section we will define the foreground galaxy and trough samples as a function of redshift, and discuss the resulting lensing measurements.

4.5.1 Redshift dependent trough selection

To study the redshift evolution of troughs we create two foreground galaxy samples, a low and a high redshift sample, which are used to select the low and high redshift troughs. These two galaxy samples need to be physically similar to ensure that the trough detection at different redshifts is not subject to bias. One requirement is that the two samples should consist of similar galaxy populations, since different kinds of galaxies might be subject to a varying amount of clustering. Another condition is that the number density of galaxies per comoving volume should be approximately equal for the two samples. In order to meet these two requirements, we define a volume limited sample of galaxies by applying a cut in redshift: $0.1 < z < 0.3$, and in absolute r-band magnitude: $M_{\rm r} < -21.0$. In this volume limited sample, all galaxies visible at the lowest redshift ($z_{\rm min} = 0.1$) are still observable up to the maximum redshift limit ($z_{\rm max} = 0.3$). Figure 4.8 shows the distribution of GAMA galaxies as a function of redshift z and absolute r-band magnitude $M_{\rm r}$, with coloured lines indicating the fiducial and volume limited galaxy samples.

When defining troughs as a function of redshift, we also need to take into account their physical shape. A visualization of the trough geometry is given by Fig. 4.9, which shows a 2D projection of the volumes that define the high and low redshift troughs. Inside these two conical frusta, the projected number density of the low (high) redshift galaxy samples will be measured in order to define the low (high) redshift troughs. The volumes need to be separated at a redshift limit $z_{\rm lim}$, which corresponds to a comoving distance limit $D_{\rm lim}$. In order to obtain a consistent definition of the troughs, $D_{\rm lim}$ is chosen in such a way that the comoving lenghts of the two volumes are equal:

$$L_{\rm low} \left(= D_{\rm lim} - D_{\rm min}\right) \, = \, L_{\rm high} \left(= D_{\rm max} - D_{\rm lim}\right) \, . \tag{4.6}$$

For our chosen redshift range: $0.1 < z < 0.3$, and the corresponding comoving distances (see Table 4.1) we find that $z_{\rm lim} = 0.198$, very close to the 'half-way' redshift of 0.2. Of course $z_{\rm lim}$ depends on our chosen values for the cosmological parameters, but this effect is $\sim 1\%$ at these low redshifts (for reasonable values of the cosmological parameters).

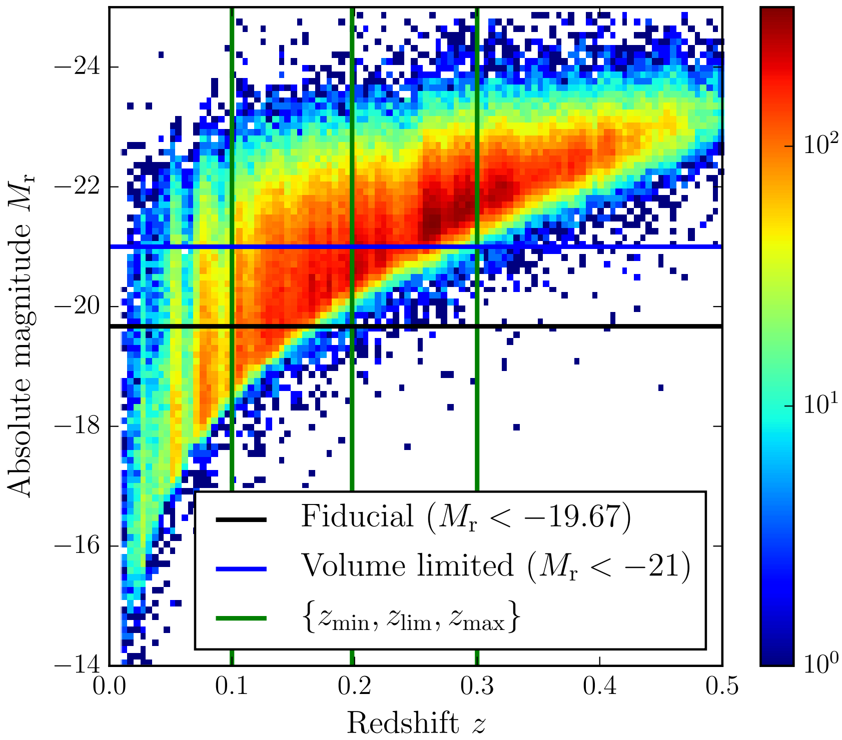

Figure 4.8: The distribution of GAMA galaxies as a function of redshift z (x-axis) and absolute r-band magnitude M_r (y-axis). The black line indicates the minimum M_r of the fiducial galaxy sample, while the blue line indicates the volume limited sample, divided into a high and low redshift sample by the green lines.

In addition to having equal lengths, the cones need to have the same radius. Selecting troughs to have equal physical radii will cause a decrease in the galaxy density at lower redshifts (i.e. later cosmic times), caused by the expansion of the Universe. Therefore, we select low and high redshift troughs that have the same *comoving* radius $R_{\rm low}$ and $R_{\rm high}$, by choosing their opening angles $\theta_{\rm low}$ and $\theta_{\rm high}$ accordingly. Here we define $R_{\rm low}$ ($R_{\rm high}$) as the comoving projected radial distance corresponding to $\theta_{\rm low}$ ($\theta_{\rm high}$) at the mean comoving distance $D_{\rm low}$ ($D_{\rm high}$) of the GAMA galaxies in the low (high) redshift sample[3]. In short:

$$R_{\rm low} \left(= \theta_{\rm low}\, D_{\rm low}\right) = R_{\rm high} \left(= \theta_{\rm high}\, D_{\rm high}\right) , \qquad (4.7)$$

[3]We use the spectroscopic GAMA redshifts for this calculation, to avoid any possible effects of photo-z scatter.

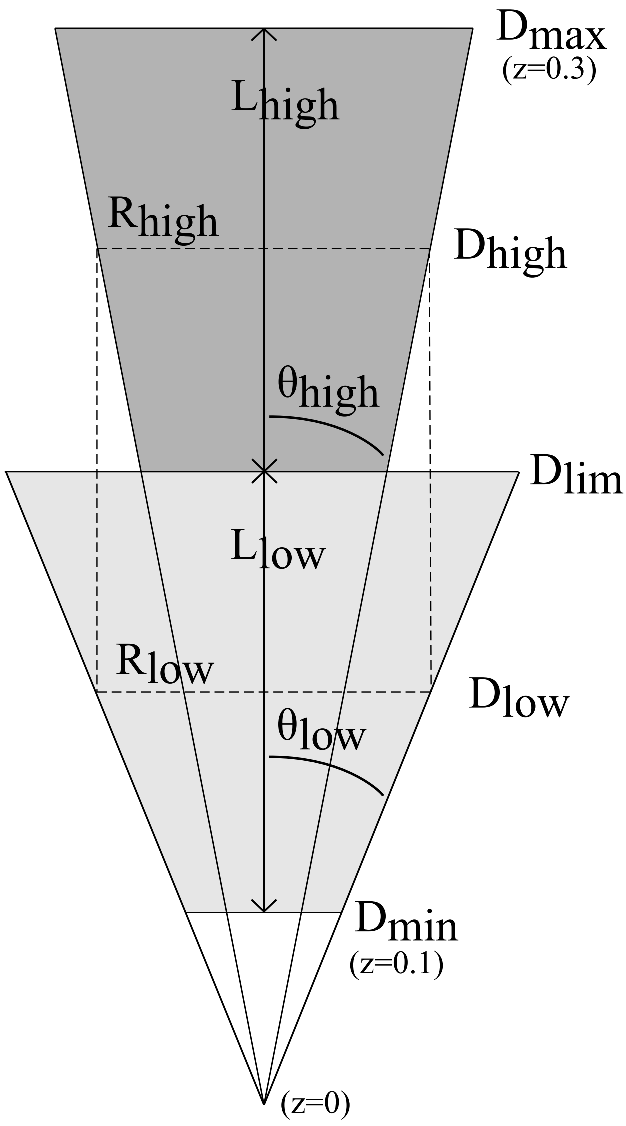

Figure 4.9: A visualization of the trough selection as a function of redshift. The two conical frusta used to define the low redshift troughs (light grey) and the high redshift troughs (dark grey) are divided at the comoving distance limit $D_{\rm lim}$. In order to avoid a biased trough selection, $D_{\rm lim}$ is chosen such that both volumes have the same comoving lenght: $L_{\rm low} = L_{\rm high}$. Moreover, the opening angles $\theta_{\rm low}$ and $\theta_{\rm high}$ of the cones are chosen such that the comoving projected radius $R_{\rm low}$ ($R_{\rm high}$) at the mean comoving distance $D_{\rm low}$ ($D_{\rm high}$) of the low (high) redshift galaxies are the same.

where $\theta_{\rm low}$ is chosen from the fiducial aperture sizes: $\{5, 10, 15, 20\}$ arcmin. We find the mean distances: $D_{\rm low} = 653.5\, h_{70}^{-1}{\rm Mpc}$ and $D_{\rm high} = 1037\, h_{70}^{-1}{\rm Mpc}$, with corresponding high redshift trough radii: $\theta_{\rm high} = \{3.152, 6.303, 9.455, 12.61\}$ arcmin. From these sizes we would like to select the smallest aperture, since this provides the shear signal with the highest S/N (as seen in Sect. 4.4.3). However, we also wish to avoid unreliable density estimates, resulting from the low number of galaxies inside smaller apertures. We therefore select a high redshift aperture size of $\theta_{\rm high} = 6.303\,{\rm arcmin}$, corresponding to $\theta_{\rm low} = 10\,{\rm arcmin}$. This ensures that $\theta_{\rm high}$ is small, but still slightly larger than our smallest fiducial aperture ($\theta_A = 5\,{\rm arcmin}$), which has proved adequate in our results and those of G16. Both opening angles correspond to a comoving projected radial distance $R_{\rm A} = 1.901\, h_{70}^{-1}{\rm Mpc}$ at their respective distances, constituting the comoving sizes of the troughs/ridges. The information on the low and high redshift galaxy samples is summarized in Table 4.1.

4.5.2 Excess surface density measurements

When the lenses have a specified redshift $z_{\rm l}$, the measured shear depends on the distance between the lens, the source and the observer. To correct for this effect, we convert the shear profile $\gamma(\theta)$ to the physical Excess Surface Density (ESD) profile $\Delta\Sigma(R)$ as a function of the physical projected separation R. The ESD is defined as the surface mass density $\Sigma(R)$, subtracted from the mean surface density $\overline{\Sigma}(< R)$ within that radius:

$$\Delta\Sigma(R) = \overline{\Sigma}(< R) - \Sigma(R) = \Sigma_{\rm crit}\gamma_{\rm t}(R)\,. \tag{4.8}$$

The conversion factor between the shear and the physical ESD is the critical surface density $\Sigma_{\rm crit}$, which is inversely proportional to the efficiency of the gravitational lensing effect. It depends on the angular diameter distance from the observer to the lens $D(z_{\rm l})$, to the source $D(z_{\rm s})$, and between the lens and the source $D(z_{\rm l}, z_{\rm s})$, as follows:

$$\Sigma_{\rm crit} = \frac{c^2}{4\pi G}\int_{z_{\rm l}+\Delta z}^{\infty} \frac{D(z_{\rm s})}{D(z_{\rm l})\, D(z_{\rm l}, z_{\rm s})} n(z_{\rm s})\,{\rm d}z_{\rm s}\,. \tag{4.9}$$

Here c denotes the speed of light and G the gravitational constant. As the lens redshifts $z_{\rm l}$ of the low (high) redshift troughs, we use the mean redshift of the low (high) redshift galaxy sample which is used to define the troughs. To estimate the redshifts $z_{\rm s}$ of the sources, we use the redshift probability distribution $n(z_\mathrm{s})$ of the full source population, determined using the direct calibration method described in Hildebrandt et al. (2017). This is done to circumvent the bias inherent in individual photometric source redshift estimates. We determine Σ_crit by integrating over the part of the source redshift probability distribution situated behind the lens ($z_\mathrm{s} > z_\mathrm{l} + \Delta z$) including a redshift buffer $\Delta z = 0.2$, following the method described in Sect. 3.2 (Eq. 9) of Dvornik et al. (2017).

Since lenses with a higher lensing efficiency ($= \Sigma_\mathrm{crit}^{-1}$) produce a stronger shear, we give them more weight in the combined ESD measurement. We incorporate Σ_crit into the total weight:

$$W_\mathrm{ls} = w_\mathrm{s} \left(\Sigma_\mathrm{crit,ls}^{-1} \right)^2 , \tag{4.10}$$

which is used to calculate our combined ESD measurement as follows:

$$\Delta\Sigma = \frac{1}{1+\mu} \frac{\sum_{ls} W_{ls} \, \Sigma_{\mathrm{crit},ls} \, \epsilon_{\mathrm{t},ls}}{\sum_{ls} W_{ls}} . \tag{4.11}$$

The correction for the multiplicative bias is weighted by the same total weight.

The angular separation range $2 < \theta < 100\,\mathrm{arcmin}$, used to measure the shear profiles in Sect. 4.4, corresponds to a physical projected separation of $0.44 < R < 22.24\,h_{70}^{-1}\mathrm{Mpc}$ at the mean angular diameter distance of the fiducial GAMA sample. We therefore measure the ESD profiles of the low/high redshift troughs for 10 logarithmically spaced bins within $0.5 < R < 20\,h_{70}^{-1}\mathrm{Mpc}$. The reason we use only half the number of radial bins, is that dividing the tracer galaxies as function of redshift results in trough profiles with a lower S/N. Although it is customary to use physical distances to measure the ESD profile around galaxies and other bound structures, the trough lensing measurements need to take the expansion of the Universe into account. We therefore translate our physical $\Delta\Sigma(R)$ profiles into the comoving surface density as a function of comoving radius, by dividing each measured $\Delta\Sigma$ by $(1 + z_\mathrm{l})^2$, and multiplying each R with $(1 + z_\mathrm{l})$.

4.5.3 Results

We measure the comoving ESD profiles of the troughs/ridges selected at different redshifts, and apply the same method of amplitude fitting and weighted stacking as discussed in Sect. 4.4.2 and 4.4.3 to both the KiDS and MICE data. The comoving radial fitting range is: $1.2\,R_\mathrm{A} < R < 20\,h_{70}^{-1}\mathrm{Mpc}$,

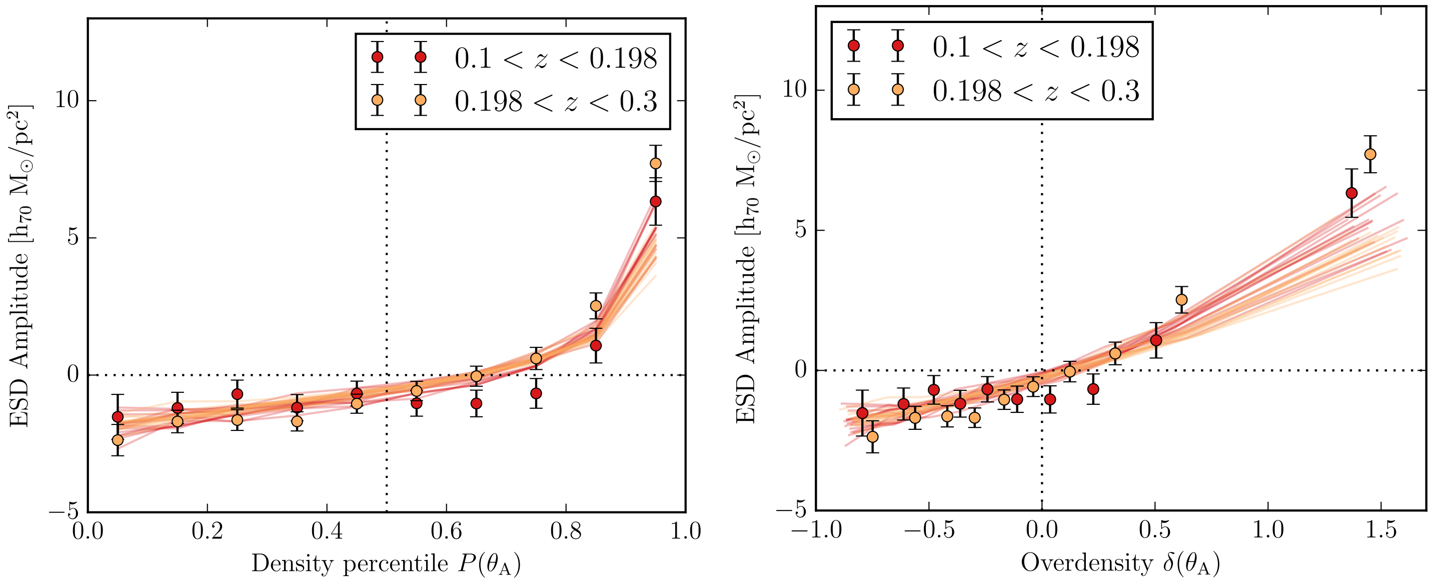

Figure 4.10: The amplitude A of the comoving ESD profiles as a function of the density percentile P (left) and overdensity δ (right), for troughs and ridges selected at two different redshifts. The observed amplitudes from KiDS (points with 1σ errors) are in reasonable agreement with those from 16 independent patches of the MICE mocks (solid lines). For the ridges ($\delta > 0$) in the MICE mocks, the amplitude is slightly higher at low redshifts. This effect, however, is not found in the observations, as we find no significant difference between the observed amplitudes at low and high redshifts.

where the maximum is based on the comoving projected distance corresponding to $\theta < 70\,\mathrm{arcmin}$ (see Sect. 4.4.1) at the mean distance of the fiducial GAMA sample. In the left panel of Fig. 4.10 we again show the best-fit amplitude A (including 1σ error bars derived from the full analytical covariance matrix) as a function of percentile P, this time for the low and high redshift troughs/ridges. For both the high and low redshift sample the shape of the $A(P)$ relation resembles that of the fiducial sample: rising gradually from negative A at low P, crossing the turn-over to positive A at $P \approx 0.6$, and peaking at $P = 1$. The observed relation is in reasonable agreement with the prediction from 16 independent patches of the MICE mocks. To assess whether there is a significant difference between the measurements of the low and high redshift troughs/ridges, we calculate the χ^2 between the amplitude difference and a null result, which is: $\chi^2 = 16.36$. Since the $A(P)$ measurements consist of $N = 10$ data-points (corresponding to a Cumulative Distribution Function with $10 - 1 = 9$ degrees of freedom) this χ^2 corresponds to 1.88σ, which means that there is no significant difference. We verify that this is in agreement with the trough results based on GAMA galaxies.

We again show the same A as a function of the overdensity δ in the right panel of Fig. 4.10. Like for the fiducial troughs, the $A(\delta)$-relation of both troughs samples is approximately linear, and crosses the turn-over point to positive A approximately at the mean density ($\delta \approx 0$) for both KiDS and MICE. Looking more closely at the center of the figure actually shows that both the KiDS and MICE results pass slightly below the origin, like we observed for the fiducial trough amplitudes with $\theta_{\mathrm{A}} = 5\,\mathrm{arcmin}$ (see Sect. 4.4.2). Because the overdensity is a measure of the galaxy number density, this non-linear relation between A and δ would, if the effect were physical, signify a discrepancy between dark and luminous matter known as galaxy bias. Again, there is no significant difference between the observed amplitudes at low and high redshift. For the MICE mocks, however, we can see that the amplitude of the low redshift ridges ($\delta > 0$) is slightly higher than that of the high redshift ridges. This is expected, since the clustering of mass increases the height of ridges at later cosmic times. It is interesting to note that, despite the observed difference in the lensing amplitude, the low and high redshift troughs/ridges span approximately the same galaxy overdensity range: $-0.8 \lesssim \delta \lesssim 1.5$.

4.5.4 Predictions for higher redshifts

The physical interpretation of the mock results in Fig. 4.10 would be that the total density of ridges increases with cosmic time. This is expected, since overdensities in the cosmic structure cluster over cosmic time, forming higher ridges. Since this mass is accreted from more underdense regions, these are expected to form deeper troughs. The latter effect, however, is not observed in the observations or the mocks between $0.1 < z < 0.3$. In order to obtain a more solid interpretation of our results, we study the predictions from the MICE-GC mocks at even higher redshifts. As our galaxy sample we use the same MICE mock galaxies with $M_{\rm r} < -21$, but without a cut in apparent magnitude such that the sample is complete at every redshift. Using this sample we perform the same redshift dependent trough selection as described in Sect. 4.5.1, but instead of dividing galaxies into two redshift bins between $0.1 < z < 0.3$ we divide them into five redshift bins between $0.1 < z < 0.6$. These five redshift slices of equal comoving length have the following redshift limits: $z_{\rm lim} = 0.1, 0.191, 0.286, 0.385, 0.489, 0.6$. As in Sect. 4.5.1 we wish to select the opening angles $\theta_{\rm A}$ corresponding to these redshifts, such that the comoving radii of the apertures are the same and none of the angles is smaller than $5\,\rm arcmin$. The chosen opening angles of the troughs, $\theta_{\rm A} = \{20., 12.85, 9.45, 7.44, 6.14\}$, correspond to the same comoving projected separation $R_{\rm A} = 3.712\,h_{70}^{-1}{\rm Mpc}$ at the mean galaxy distance in each redshift bin.

We perform the same measurement of the comoving ESD profiles, and fit the same $A/\sqrt{R}$ function to the results. In the left panel of Fig. 4.11 we again show the best-fit amplitude A of as a function of percentile P, this time for mock troughs/ridges in the five redshift bins. In the highest percentile bin ($0.9 < P < 1$) we can see that the difference that was barely visible in Fig. 4.10 has become a significant trend: as the redshift increases to $z = 0.6$, the ridge amplitude decreases. This trend can be better appreciated in the right panel of Fig. 4.11, which shows the amplitude as a function of overdensity δ: the absolute value of A clearly decreases with redshift for the ridges. This effect is even slightly visible for the troughs where, except for the second redshift bin ($0.191 < z < 0.286$), A continues to increase with z. But while the comoving ESD amplitude range spanned by the troughs/ridges increases with cosmic time, the span of the galaxy overdensity range slightly decreases for the ridges. This apparent increase in the density contrast of the total mass distribution while that of the galaxy distribution decreases, might again signify non-linear galaxy bias. Unfortunately, as seen in Sect. 4.5.3, it is not yet possible to observationally mea-

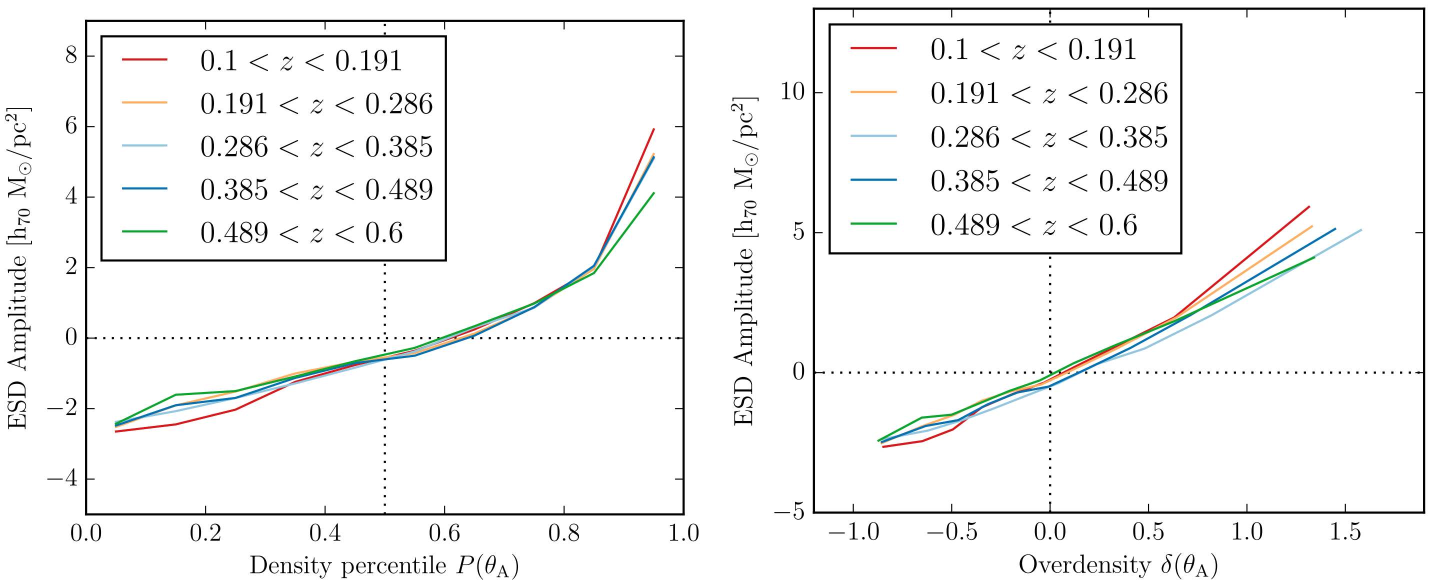

Figure 4.11: The amplitude A of the comoving ESD profiles from MICE mocks as a function of the density percentile P (left) and overdensity δ (right), for troughs and ridges selected at five different redshifts between $0.1 < z < 0.6$. For both troughs and ridges the redshift evolution, that was hinted at by the results at low redshifts, appears to be a continuing trend. Except for the erratic behaviour in the fourth redshift bin, the covered range of A steadily decreases with redshift. This is expected from the clustering of mass with cosmic time, which causes massive ridges to accrete mass from the low density troughs. However, the covered range of δ seems to slightly increase with redshift. If physical, this would signify an increase in the total density contrast with cosmic time, but a decrease in the contrast of the galaxy density distribution.

sure these small effects at high redshifts using the current lensing surveys.

4.6 Discussion and conclusion

We use the Kilo-Degree Survey (KiDS) to perform a weak gravitational lensing study of troughs: circular projected underdensities in the cosmic galaxy density field, following up on the work by Gruen et al. (2016, G16). We define the troughs using two different foreground galaxy samples: 159,519 galaxies from the equatorial fields of the Galaxy and Mass Assembly (GAMA) survey, and a sample of 309,021 KiDS galaxies that is limited to photometric redshift $z_{\rm ANN} < 0.5$ and apparent magnitude $m_{\rm r} < 20.2$ in order to mimic the GAMA selection. Both galaxy samples are limited to an absolute magnitude $M_{\rm r} < -19.67$ in order to mimic the mock galaxy sample from the MICE Grand Challenge (MICE-GC) lightcone simulation, which is used to interpret our results. Following the fiducial trough definition of G16 (apertures with a density percentile $P(\theta_{\rm A}) < 0.2$), we detect a gravitational lensing signal with a signal to noise of $|S/N| = 12.3$ for the KiDS foreground sample and 12.0 for GAMA. Since the current KiDS area already provides a more significant trough lensing detection than the GAMA survey, we mainly use KiDS for this work (although we confirm all our results using GAMA). As the KiDS survey progresses in the coming years, the available area will become even larger and less irregular. The coming KiDS data release, which aims to make a contiguous area of $900\,\deg^2$ available for lensing studies, will likely reduce the systematic lensing effects found at large scales and increase the detection significance of the trough signal (at most by a factor of $\sim \sqrt{900/180} = 2.24$ compared to GAMA).

In addition to stacking only the most underdense/overdense 20% of the apertures, we study troughs and ridges (overdensities) as a function of their galaxy number density $n_{\rm g}$. By fitting the simple function $\gamma(\theta) = A/\sqrt{\theta}$ to the lensing signal in bins of increasing $n_{\rm g}$, we obtain the amplitude A of troughs and ridges as a function of density percentile P and overdensity δ. We discover that the turning point between negative and positive A is situated at $P \approx 0.6$ (and not at the median density $P = 0.5$), while $A(\delta)$ does generally pass through the origin (the mean density $\delta = 0$). This indicates that the non-linearities in the density field caused by structure formation, which are shown by the skewed distribution of $n_{\rm g}$ (see Fig. 4.1), are reflected in the total (baryonic + dark matter) density distribution measured by gravitational lensing. As expected, these non-linearities are more prominent at smaller scales, i.e. for smaller trough radii. This conclusion is supported by mock trough profiles obtained from the MICE-GC lightcone simulation, which show exactly the same trend.

We also use the amplitude A and its 1σ error δA to define the signal to noise (S/N) of the lensing profiles as $A/\delta A$. The S/N as a function of P is used as a weight to optimally stack the shear profiles of all troughs/ridges, in order to obtain the highest possible detection significance. The optimally stacked lensing signals have $|S/N| = \{17.1, 14.8, 10.0, 7.6\}$ for troughs with a size of $\theta_{\rm A} = \{5, 10, 15, 20\}\,{\rm arcmin}$, significantly higher than that of the fiducial trough definition ($|S/N| = \{12.3, 10.7, 8.4, 5.7\}$). Inspecting the optimally stacked trough and ridge profiles shows that the shear profiles of ridges are much stronger than those of troughs, especially for the smallest trough radius. This finding, which is in agreement with the results from the MICE-GC mocks and the observations from G16, again reveals the skewness of the total mass density distribution.

Finally we try to observe physical evolution of the density field, by performing the trough selection in two redshift bins. We create a volume limited sample of foreground galaxies ($z < 0.3$ and $M_{\rm r} < -21$), and split it into a low ($0.1 < z < 0.198$) and high ($1.198 < z < 0.3$) redshift sample of equal comoving length. By adjusting the opening angle $\theta_{\rm high}$ of the high redshift apertures, we ensure that the comoving projected radius of the troughs is identical at both redshifts: $R = 1.901\,h_{70}^{-1}{\rm Mpc}$. The measurement of the Excess Surface Density (ESD) profiles provides the physical surface density distributions of the troughs/ridges, taking into account their distances to the KiDS source galaxies. After converting physical to comoving ESD profiles to correct them for the expansion of the Universe, we do not observe a significant difference between the trough/ridge amplitudes A as a function of P and δ. Applying the same method to 16 independent patches of the MICE-GC mock catalogue provides a reasonable agreement with the observation, although the $A(\delta)$ relation of the mocks reveals a slight decrease in the lensing amplitude of ridges with redshift. This increase in ridge height with cosmic time is expected from the effects of clustering.

The question remains whether this trend continues at higher redshifts, and whether the effects of clustering can also be observed in troughs. We therefore use the MICE mock catalogue to gain more insight into our finding, by extending our measurement to five redshift bins between $0.1 < z < 0.6$. The comoving ESD amplitude of the mock ridges continues to decrease with redshift, indicating that the increasing ridge height with cosmic time is an actual trend. In the mock measurements at high redshifts, we can even find a trace of the corresponding deepening of troughs with cosmic time.

Future efforts using the increasing KiDS area and DES area+depth, or upcoming surveys like Euclid and the LSST, might be able to observationally measure this effect.

Acknowledgements

This research is based on data products from observations made with ESO Telescopes at the La Silla Paranal Observatory under programme IDs 177.A-3016, 177.A-3017 and 177.A-3018, and on data products produced by Target OmegaCEN, INAF-OACN, INAF-OAPD and the KiDS production team, on behalf of the KiDS consortium. OmegaCEN and the KiDS production team acknowledge support by NOVA and NWO-M grants. Members of INAF-OAPD and INAF-OACN also acknowledge the support from the Department of Physics & Astronomy of the University of Padova, and of the Department of Physics of Univ. Federico II (Naples).

GAMA is a joint European-Australasian project based around a spectroscopic campaign using the Anglo-Australian Telescope. The GAMA input catalogue is based on data taken from the Sloan Digital Sky Survey and the UKIRT Infrared Deep Sky Survey. Complementary imaging of the GAMA regions is being obtained by a number of independent survey programs including GALEX MIS, VST KiDS, VISTA VIKING, WISE, Herschel-ATLAS, GMRT and ASKAP providing UV to radio coverage. GAMA is funded by the STFC (UK), the ARC (Australia), the AAO, and the participating institutions. The GAMA website is `www.gama-survey.org`.

This work has made use of PYTHON (`www.python.org`), including the packages NUMPY (`www.numpy.org`), SCIPY (`www.scipy.org`) and IPYTHON (Pérez and Granger 2007). Plots have been produced with MATPLOTLIB (Hunter 2007). The mock shear profiles from MICE are computed using TREECORR (`https://pypi.python.org/pypi/TreeCorr`).